M2LW-18OR0402152
PNNL-27923

Light Water Reactor Sustainability Research and Development

Fracture Resistance of Cast Stainless Steels after Thermal Aging for up to 10000 Hours

Cast Stainless Steel Aging (LW-18OR040215)

September 2018

U.S. Depart of Energy

Office of Nuclear Energy

Department of Energy/Office of Nuclear Energy
LWR Sustainability R&D
Cast Stainless Steels Aging (WP#: LW-18OR040215)

Fracture Resistance of Cast Stainless Steels after Thermal Aging for up to 10000 Hours

Thak Sang Byun (PI), David A. Collins, Emily L. Barkley, Timothy G. Lach
Pacific Northwest National Laboratory

Feng Yu
Electric Power Research Institute

Pacific Northwest National Laboratory
operated by
Battelle
for the
U.S. Department of Energy
under contract DE-AC05-76RL01830

TABLE OF CONTENT

LIST OF TABLES AND FIGURES

Fracture Resistance of Cast Stainless Steels after Thermal Aging for up to 10000 Hours

Thak Sang Byun (PI), David A. Collins, Emily L. Barkley, Timothy G. Lach
Pacific Northwest National Laboratory
Feng Yu
Electric Power Research Institute

ABSTRACT

This work package, Cast Stainless Steel Aging, aims to achieve a comprehensive scientific understanding on the aging and failure phenomena in cast austenitic stainless steels (CASSs) using holistic experimental and modeling means and to provide a practical and science-based model to predict the degree of thermal degradation of CASS components in extended-term operations. The test materials in the project include four model CASSs (CF3, CF3M, CF8, and CF8M), four EPRI-provided CASSs (CF3, two CF8s, and CF8M), and two reference wrought materials (304L and 316L), which contain a wide variety of δ-ferrite contents (2–33%). These materials have been thermally aged at two light water reactor (LWR)-relevant temperatures (290 and 330°C) and at two accelerated-aging temperatures (360 and 400°C) for up to three years. In the fiscal year, the fracture toughness testing and J-R curve calculation were completed for the ten CASS and wrought materials aged up to 10,000 hours. This report is to present the results of the static fracture (J-R) testing for the model and EPRI-provided CASS materials after thermal aging up to 10,000 hours. First, a new aging parameter (A) was defined to present the aging degradation of mechanical properties against the common variable. This definition is used to scale an aging time at a temperature to the effective aging time at a reference temperature based on Arrhenius equation, which is a rate theory equation for thermally activated mechanisms. Second, the fracture test results are presented in the forms of fracture resistance (J-R or J-Δa) curves, K_{JQ} versus A curves, and tabulated crack length and fracture toughness data for ~460 fracture tests. Third, the fracture test results indicate that the fracture toughness tends to increase in early aging; after a short time, however, it decreases with aging parameter at a rate depending on the volume fraction of δ-ferrite. Overall, the decrease of static fracture toughness due to thermal aging is less significant than that of Charpy impact energy, which usually is measured as the reduction of upper shelf energy and shift of ductile-brittle transition temperature. Finally, a preliminary conclusion is derived for the static fracture behavior of aged CASS materials; which states that the cast stainless steels with δ-ferrite contents less than ~20% will not be subjected to a significant reduction of static fracture toughness or embrittlement over the extended lifetimes of reactors.

1. INTRODUCTION

The coolant system of a pressurized water reactor is built to remove thermal energy from the reactor core and transfer that energy to the steam turbine, and therefore its components are extensively exposed to the persistently damaging environments of high temperature (270–330°C), high pressure (~15.5 MPa), corrosive coolant chemistry, and radiation [1]. The cast iron-chromium-nickel (Fe-Cr-Ni) alloys with mostly 300-series stainless steel compositions and

austenite (γ)–ferrite (δ) duplex structures have been used for the majority of the components of the primary coolant system because of their high heat and corrosion resistances. Particularly, those cast austenitic stainless steel (CASS) materials are most commonly used for the massive primary coolant system components such as coolant piping, valve bodies, pump casings, and piping elbows. Since a large number of CASS components are installed in every nuclear power plant and replacing such massive components should be prohibitively expensive, any significant degradation in mechanical properties (cracking resistance, in particular) that affects the structural integrity of CASS components would raise a serious concern on the performance of entire nuclear power plant [1,2]. The past researches on the thermal degradation of CASS materials, however, have been performed for the CASS materials after aging mostly in selected (i.e., highly accelerated) conditions as well as for some limited properties that often cannot be directly related to the integrity or failure of CASS components. In fact, the existing prediction models and criteria for the integrity of CASS components were established based on the plant operation experiences [2], which naturally lacks ability for prediction of system integrity during the proposed extended-term operations. Therefore, the ongoing research, Cast Stainless Steel Aging, aims to systematically expand scientific understanding and property database on thermal-aging induced degradation in CASSs, and ultimately, to provide a knowledge-based, conclusive prediction for the integrity of CASS components during the service life extended up to and beyond 60 years [1].

The CASS alloys generally have austenite (γ)–ferrite (δ) duplex structure which results from the casting process consisting of alloy melting and pouring or centrifugally injecting liquid metal into a static or spinning mold [3-6]. Although the commonly used static and centrifugal casting processes enable the fabrication of massive components with proper resistance to environmental attacks, the alloying and microstructural conditions are not highly controllable in actual fabrication, especially in the casting processes of massive components. Therefore, the actual microstructure of a CASS component varies widely with its composition, casting method, and wall thickness (i.e., cooling rate). The most common cast stainless alloy grades include the CF3 and CF8 alloy families with nominally ~19% Cr and ~10% Ni and 3–30% δ-ferrite [7-15]. The minor phase (i.e., the δ-ferrite phase) is inevitably formed during the casting process, and is in a non-equilibrium state subject to detrimental changes during exposure to elevated temperature and/or radiation.

The degree of aging degradation in a CASS alloy is determined by the chemistry and processing route of the alloy [7-13] because these determine the amount and distribution of δ-ferrite and small precipitates. The primary fracture mechanism observed in a thermally embrittled duplex stainless steel is cleavage initiation at the aged δ-ferrite followed by propagation through separation of ferrite-austenite phase boundary. This cracking mechanism could be caused or enhanced by various microstructural changes during thermal aging, such as formation of a Cr–rich α'-phase through the spinodal decomposition of δ-ferrite, precipitation of G-phase and $M_{23}C_6$ carbide, and additional precipitation and growth of carbides and nitrides at ferrite-austenite phase boundaries [6-24]. In the austenite matrix, on the other hand, thermal aging induces various precipitations but usually causes a negligible to moderate effect on the properties of the phase [9-12].

This research project has investigated the thermal aging effects in four model CASSs (CF3, CF3M, CF8, and CF8M) and four EPRI-provided CASSs (CF3, two CF8s, and CF8M). These materials have been thermally aged at LWR-relevant temperatures (290 and 330°C) as well as at accelerated-aging temperatures (360 and 400°C) to cover a large range of aging parameter and to

validate the accelerated aging technique by comparison. To quantify the degradation of CASS materials during thermal aging, mechanical properties (fracture toughness, tensile strength and ductility, and Charpy impact energy) have been evaluated for eight CASS materials and two wrought stainless steels after aging at 290 – 400°C. Lately, the fracture toughness testing and J-R curve calculation were completed for all ten materials aged up to 10,000 hours. This report is to present the fracture toughness data from testing campaign as well as to draw a preliminary prediction on the overall static facture behavior of the CASS materials in extended operations.

2. EXPERIMENTAL

2.1. Test materials

The most common CASS materials used in nuclear power plants are the family of CF grades, which normally have key compositions of ~19% Cr and ~10% Ni and austenitic(γ)-ferritic(δ) duplex structures [6-9]. The volume fraction of δ-ferrite formed during the casting process is dependent on the cooling rate, which is usually influenced by the size of the CASS component and casting method (typically static casting or centrifugal casting) as well as the composition of the alloy. Nuclear grade CASS alloys typically contain 3–30% δ-ferrite in an austenite matrix [1]. Since the volume fraction of retained δ-ferrite is the most influential parameter related to the degree and rate of aging degradation, eight cast stainless steels containing a wide range of δ-ferrite content(4–33%) and two reference wrought alloys with < 3% δ-ferrite were tested in this research. Table 1 lists the chemistries of the four model and four EPRI-provided CASS alloys, along with the reference compositions in ASTM specification for these alloys [6]. The primary controlled-elements are C and Mo; the CF3 and CF3M have a lower carbon content (< 0.03 wt.%), while the CF3M and CF8M are alloyed with 2–3 wt.% Mo. The four model CASS alloys (CF3, CF3M, CF8, and CF8M) have been produced in the form of small (Ø~10 cm × L~40 cm) ingots to have relatively low δ-ferrite volume fractions (4–16%), while the four EPRI-provided alloys (CF8M(K23), CF8(S43), CF3(Z21), and CF8(ELB)) were taken from simulated or vintage components in EPRI's storage yard in Charlotte, NC; these materials have higher δ-ferrite contents (11–33%). All chemical composition data was produced by Dirats Laboratories in Westfield, MA. Table 2-1 also includes the information on casting routes and dimensions of the original components.

Table 2-1. Chemical compositions of model and EPRI-provided CASS materials. The amounts are given in wt.% for main alloy elements or in ppm for trace elements, i.e., C, S, O and N.

Grade (Equivalent Wrought Steel or Component)	Fe	Cr	Ni	Mn	Mo	Si	Cu	Co	V	P	C	S	O	N
CF3 (304L) (~10 cm dia. Ingot) Model/Static casting	Bal.	19.17	8.11	1.44	0.34	0.99	0.41	0.18	0.07	0.029	262	324	204	1020
CF3M (316L) (~10 cm dia. Ingot) Model/Static casting	Bal.	19.28	9.81	1.14	2.30	1.22	0.28	0.15	0.05	0.033	284	253	224	838
CF8 (304) (~10 cm dia. Ingot) Model/Static casting	Bal.	18.72	8.91	1.10	0.29	1.27	0.29	0.15	0.05	0.026	665	376	161	606
CF8M (316) (~10 cm dia. Ingot) Model/Static casting	Bal.	18.52	10.38	0.65	2.33	1.02	0.33	0.17	0.06	0.031	433	243	207	1020

CF8 (ELB) (20.3 cm thick elbow) Vintage/Static casting	**Bal.**	**21.20**	**8.45**	**0.61**	**0.18**	**1.78**	**0.16**	**0.04**	**0.02**	**0.017**	**360**	**60**	**53**	**411**
CF8 (S43) (8.6 cm thick piping) Vintage/Static casting	**Bal.**	**20.01**	**8.61**	**0.57**	**0.30**	**1.31**	**0.07**	**0.08**	**0.02**	**0.031**	**590**	**130**	**36**	**450**
CF8M (K23) (6.9 cm thick piping) Simulated/Centrifugal casting	**Bal.**	**20.77**	**10.16**	**0.95**	**2.51**	**0.85**	**0.39**	**0.16**	**0.07**	**0.032**	**590**	**220**	**25**	**1500**
CF3 (Z21) (10.4 cm thick piping) Vintage/Centrifugal casting	**Bal.**	**20.69**	**9.57**	**0.89**	**0.14**	**1.10**	**0.10**	**0.03**	**0.04**	**0.023**	**220**	**30**	**53**	**572**

For this research, these eight CASS materials have been thermally aged in large capacity furnaces set at 290, 330, 360, and 400°C since either year 2014 or 2015, along with the reference wrought stainless steels 304L and 316L, and three weld alloys. Except for the weld alloys, the aging time for the materials has reached 30 kh in this fiscal year and characterization of the 30 kh aged materials is underway. This report presents the fracture toughness datasets for four model alloys aged for 0h, 1.5 kh and 10 kh and for the four EPRI-provided alloys after aging for 0h and 10 kh.

Table 2-2 lists the ferrite content of the CASS alloys in the as-cast condition. The ferrite numbers (FNs) were measured from Charpy impact or three-point bend bar fracture specimens using a ferrometer (model: Feritscope-FMP30C of Fisher Co.). For each alloy, many (30–50) FNs were measured and statistically analyzed to provide the data in the table; the volume fraction data listed was converted from the FN measurements. Among the model alloys, the CF3M alloy has the highest volume fraction average of 15.7%, which is followed by CF3 with 12.4%. The CF8 and CF8M contain relatively low δ-ferrite content, 4.7 and 5.6% respectively. These model alloys were likely produced at rather high cooling rates as the ingots were only ~10 cm diameter. Table 2-2 also shows that the centrifugal cast CF3 (Z21, Z43) and CF8M (K23, K25) pipings have similar δ-ferrite contents (~12%) as those of the model alloys CF3 and CF3M (< 16%). Both the static cast materials, CF8 (pipings S43, S52) and CF8 (elbow ELB), however, contain much higher δ-ferrite contents (25–33%). In particular, the CF8 (ELB) alloy has the highest δ-ferrite content (33%) as its cooling was the slowest due to its size (~20 cm thick) and its static casting production method. The casting method is believed to be the most influential factor related to δ-ferrite content, which is followed by the Mo and C content. The chemical composition and cooling rate determine the microstructure after casting, especially the volume fractions of the ferrite (δ) and austenite (γ) phases. The δ-ferrite content can vary widely with the thermal history of the casting process since the cooling rate during the ferrite formation region of the phase diagram might determine the total exposure time for ferrite formation.

It was also observed that these initial FNs decrease with increased thermal aging. This phenomenon is, however, not discussed further in this report since the cause for the decrease in FN by aging treatment is not well explained.

Table 2-2. Content of δ-ferrite measured in the as-cast condition (the volume fraction data (in %) was calculated from FN measurements)

Grade	FN	STDEV (FN)	Vol.%	STDEV (Vol.%)
CF3 (Model Alloys)	11.4	0.88	**12.4**	1.02
CF3M (Model Alloys)	14.6	1.53	**15.7**	1.76

CF8 (Model Alloys)		4.2	1.01	**4.7**	1.17
CF8M (Model Alloys)		4.9	0.52	**5.6**	0.60
CF8M Simulated/Centrifugal	K23	10.4	1.69	**11.4**	1.94
	K25*	11.8	1.82	**12.9**	2.09
CF8 Vintage/Static	S43	24.7	3.13	**25.1**	3.57
	S52*	31.1	3.35	**30.6**	3.82
CF3 Vintage/Centrifugal	Z21	10.8	2.21	**11.8**	2.53
	Z43*	11.3	2.60	**12.3**	2.97
CF8 (ELB) Vintage/Static (Elbow)		34.0	3.75	**33.0**	4.26

**Only tensile test data in as-cast condition are included in this report.*

2.4. Fracture toughness testing and data analysis

Single-edge bend bar (SEB) specimens were used for static fracture testing; the geometry of these specimens is shown in Figure 2-1. The bars have a center notch approximately 3.5mm deep and side grooves approximately 1.5mm deep on each side of the notch. The purpose of these side grooves was to enhance stress triaxiality (or strain constraint) in the three-point bend loading condition and to guide the direction of crack propagation, which can otherwise be very erratic in ductile materials. For precracking and static fracture testing these samples were loaded in a three-point bend mode, with the span of the bend being approximately 40mm.

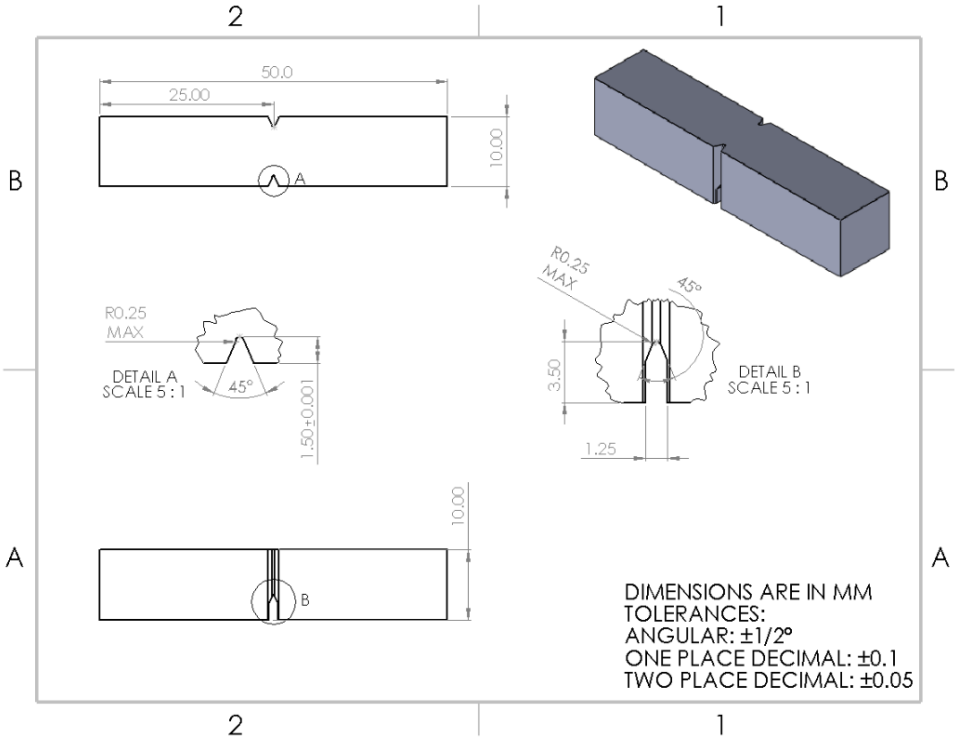

Figure 2-1. SEB specimen geometry showing a 15% side groove on each side.

The SEB specimens were precracked in air at room temperature by cyclically loading

between 2100N and 100N at 10 Hz. In order to achieve a desired precrack length of approximately 5mm, or half the width of the specimen (or initial crack ratio $a/w \approx 0.5$), the displacement mean was monitored until it had increased by 70-100 microns; this generally occurred between 30-100k cycles. The maximum load was then decreased to 1100N and an additional 10k cycles were applied to sharpen the crack tip to maximize localized stress at the crack tip.

Static fracture testing was performed at a constant displacement rate using a TestResources servo-electric testing system equipped with a high temperature furnace. Each sample was heated in the zero-load condition in air to the desired temperature; the temperature of the sample was monitored directly via a thermocouple fed through the furnace. Once the sample was within ±3°C of the targeted test temperature, a 100N load was applied and the relative displacement was set to 0mm for initialization. The sample was then tested at a displacement rate of 0.005mm/sec and a data acquisition rate of 5 Hz. The load was monitored until the maximum load had been reached; the testing machine was then programmed to stop the test once the load had dropped below 55% of the peak load. For this set of tests, the nominal test temperatures were room temperature (typically 22°C), 200°C, 290°C, 330°C, 360°C, and 400°C.

After testing, the samples were heat tinted to mark the final crack length, then the samples were manually bent in half until broken completely. The initial and final crack length of each sample was measured by examining the fracture surfaces under a low-magnification optical microscope equipped with a digital camera; the length of the crack was measured in pixels and then converted to mm. As the crack fronts were not perfectly straight, initial and final crack lengths were calculated using a weighted average in accordance with the ASTM standard method. Nine evenly-spaced points were measured across the initial and final crack fronts, two along the side grooves and seven in between. The lengths of the crack at the side grooves were weighted each at ½, then all the lengths were averaged over a factor of 8.

Prior to calculating the J-R curves and fracture toughness values, the raw data was first smoothed to 100±30 load-displacement data points by averaging the raw data points over the appropriate data spans. Once the raw data had been smoothed, the J-R curve and fracture toughness values were calculated using a modified version of the curve normalization method as outlined in ASTM E1820; this was the only available method as no external displacement gauge was used. As described in earlier publications, modifications were made in a few places to accommodate the simplification in the data acquisition; the main modification made in the J-R data calculation regards the use of displacement data either from the built-in displacement device or from cross-head movement. Further, as the cast and wrought stainless steel specimens were relatively softer than those of which the ASTM method is generally used for, and because the subsize SEB specimen design, even with such deep side grooves, limited the degree of constraint at crack tip, a couple of modifications had to be made in the calculations to compensate for the excessive ductility. First, the true ultimate tensile stress was used in the calculation of the flow stress as opposed to the engineering ultimate tensile stress. This is a correction to account for the high uniform ductility of stainless steels. Second, the final fracture length used in the calculations often differed from the optically measured final fracture length.

This occurs because the iterative calculations which determine the final calculated crack length assumes a continuous normalized load-displacement curve; in order to reconcile these two conditions, the calculated final crack length is often different from the actual value.

3. EFFECTS OF THERMAL AGING ON FRACTURE TOUGHNESS

Thus far, more than 450 fracture toughness tests in total have been performed in the present aging effect research, which includes the baseline fracture tests for the as-cast and as-wrought stainless steels and the fracture tests after aging for 1.5kh and 10kh at four temperatures, which are newly reported in this report. In the chapter, only selected sets of J-R curves and fracture toughness data are displayed and discussed for elucidating the effect of thermal aging: (i) Figures 3-1 through 3-10 represent selected J-R curves for all 10 materials tested at 330°C. (ii) Figures 3-11 through 3-20 compare the K_{JQ} versus A (aging parameter) curves in each alloy to display the effect of thermal aging on fracture toughness; the data displayed in this section are for the specimens tested at 22°C, 290°C, and 400°C only. A full list of fracture toughness values for each alloy at each testing and aging condition is given in Appendix A. The tables in the appendix include both the J-integral value and the stress intensity factor (K) value for each specimen, which are determined at the intersections of the J-R curve with the 0.1 mm and 0.2 mm offset lines of its crack blunting line.

3.1. Selected fracture resistance (J-R) curves

The objective of this project is to evaluate the effect of thermal aging on the mechanical properties of the cast and wrought stainless materials, which are measured by uniaxial tensile, Charpy impact fracture, and static fracture testing. The J-R curve is a useful tool for determining the static fracture resistance of a material, which is essentially a measure of the interplay between crack growth and energy absorbed by the material. In this section, examples of J-R curves of aged and non-aged cast stainless steels are displayed. J-R curves of wrought alloys are also displayed in this section as reference datasets.

Though there are several microstructural factors that may determine the toughness of the cast materials, one of the most prominent and easy to quantify is the amount of the δ-ferrite in the material formed at high temperature during the casting process. As the δ-ferrite phase is highly susceptible to spinodal decomposition, G-phase formation, and segregation at its interface with austenite, all of which are causes of reduced mechanical performance or embrittlement, the susceptibility of a cast material to aging degradation will be strongly intertwined with the amount of δ-ferrite present. Therefore, the amount of initial δ-ferrite, aging condition, and test temperature will be the key parameters discussed in the following two sections.

As shown in Figures 3-1 and 3-2 for the wrought alloys 304L and 316L (chemically equivalent to CF3 and CF3M, respectively), both materials show excellent fracture resistance regardless of the aging conditions. These materials have very low ferrite contents (< ~3%), and so any degradation effects within that part of the microstructure are unlikely to have a significant effect on the macro-scale mechanical properties; statistical variability between specimens would be the factor most responsible for the differences between the curves. Only insignificant or slow degradation with thermal aging is observed for these materials; the J-R curves of the 304L and 316L curves do show some dependence on the aging conditions, with the pristine and 10kh/290°C materials showing the best performance and the 10kh/400°C showing the worst. Also, the increased presence of molybdenum may have some effect on the 316L since molybdenum is a ferrite-stabilizing element. Regardless, all the materials in Figure 3-1 and 3-2 show excellent properties.

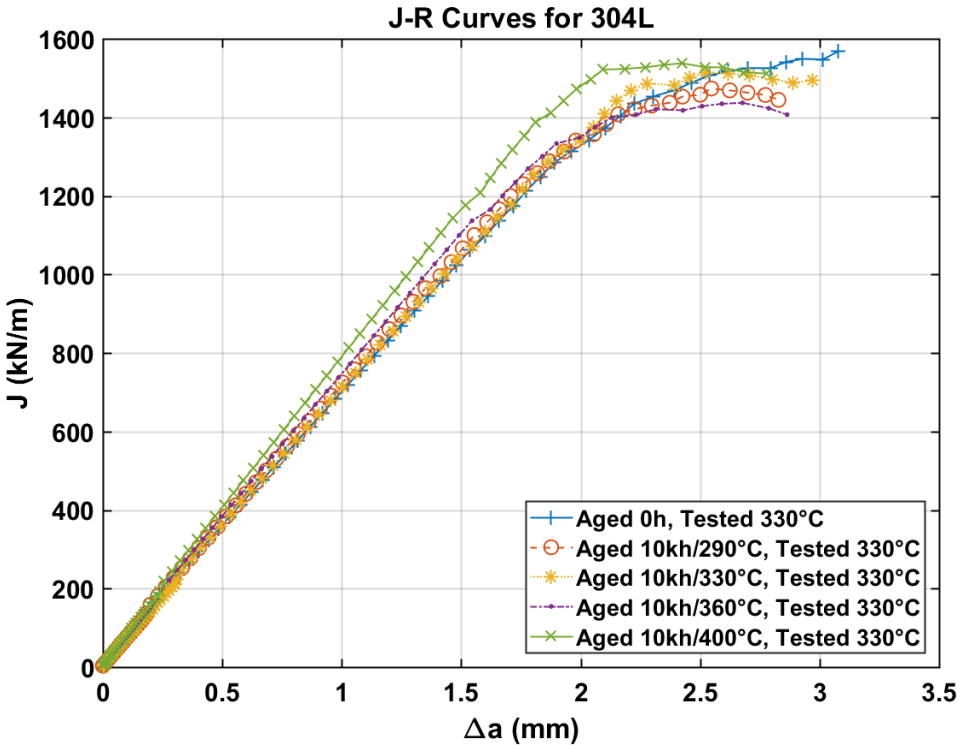

Figure 3-1. Selected J-R curves for the wrought alloy 304L, which was aged for 10kh at four different temperatures and tested at 330°C.

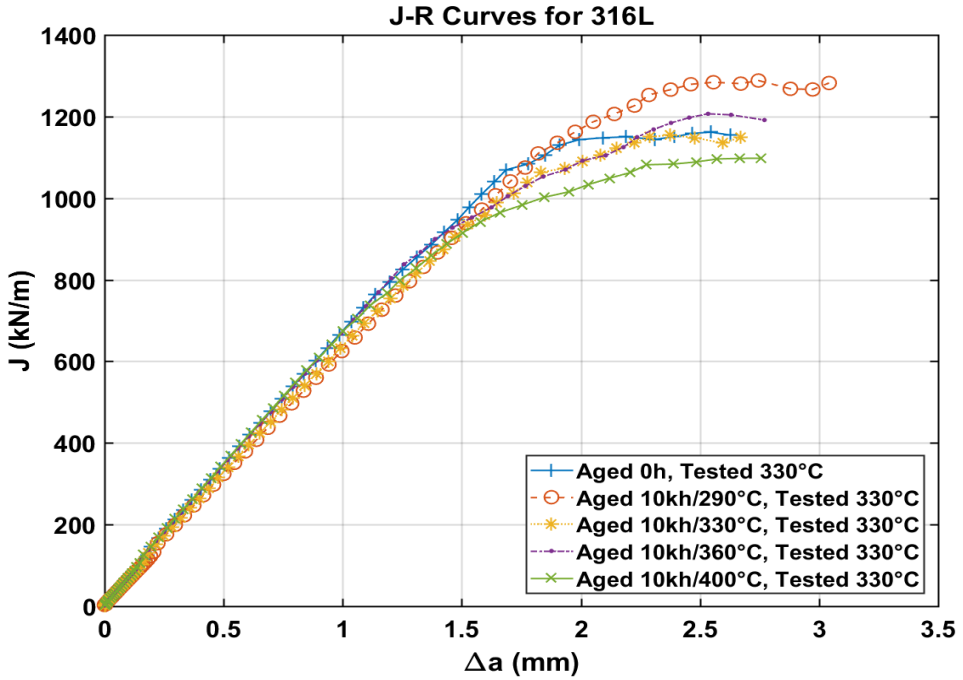

Figure 3-2. Selected J-R curves for wrought alloy 316L, which was aged for 10kh at four different temperatures and tested at 330°C.

Example J-R curves of the model CASS materials (CF3, CF3M, CF8 and CF8M; static cast alloys) are displayed in Figures 3-3 through 3-6, respectively. To understand the detailed fracture resistance behavior of these model alloys, it needs to be considered that the relatively high cooling rate during casting due to the small ingot diameters (typically ~10 cm) resulted in low δ-ferrite contents and fine grain structures. In the cast alloys with low δ-ferrite contents the effect of degradation of δ-ferrite phase is not expected to be a predominant component in the macroscopic property changes; which might be similarly contributed by some minor effects such as softening in austenite phase and stress relaxation. Therefore, the dependence of fracture toughness on the aging conditions may not be simply proportional to the main microstructural processes in the δ-ferrite, but rather may be more complex and involve multiple microstructural features and processes.

Figure 3-3 shows the J-R curves for non-aged CF3 (~12% δ-ferrite) tested at 330°C. Relative to its wrought material counterpart (304L), it has considerably lower fracture resistance overall. Even an elevated level of ferrite has an adverse effect on the fracture toughness, regardless of whether or not the material has degraded. When compared to the J-R curve of non-aged CF3, the 290°C and 330°C aged materials actually show better resistance to crack propagation over the whole crack extension range; the J-values of the 360°C and 400°C aged materials become higher in the larger crack range as well. It is obvious that the thermal aging of cast materials sometimes results in thermally induced toughening, albeit the degree of toughening is not significant and it might only improve the properties of the materials with low amounts of δ-ferrite. This could be attributed to several factors regarding the non-equilibrium as-cast status of the material, including possible thermal softening due to diffusion and dislocation movement and resultant relaxation of internal stresses. It is also possible that the 290°C and 330°C materials had a lower ferrite content than the pristine materials and were therefore less affected by its presence, even possibly to the point that the expected effects of thermal degradation were offset.

Figure 3-4 shows selected curves for CF3M (~16% δ-ferrite), a high-molybdenum version of CF3 and the chemical counterpart of 316L. For this material, there doesn't appear to be any apparent correlation between aging temperature and fracture resistance. Though the pristine material shows somewhat better fracture resistance at room temperature, the temperature-dependent interplay between strength and ductility can make these properties more unpredictable at elevated temperatures. Though an embrittled material may be less tough than a pristine material at room temperature, the cause of embrittlement can improve that material's resistance to softening at elevated temperature, giving it superior properties relative to the non-aged material.

Figure 3-5 displays the J-R curves for CF8 (~5% δ-ferrite) tested at 330°C. Its carbon content is higher than that of CF3, but its molybdenum amount is lower. On the whole, its qualitative behavior is similar to that of CF3 and CF3M. Unlike the two previous cast materials, the pristine material shows the best fracture resistance, while the worst is arguably that of the 400°C aged material, though it could be argued the 330°C aged material is worse, depending on what crack length is considered. As with the other materials, the correlation between δ-ferrite content, aging condition, and fracture properties is complex. However, in this case, the ferrite content of these materials is relatively low, whereas for CF3 and CF3M the ferrite content is higher. The CF3 and CF3M contrast with the CF8 in that for the former two materials the pristine versions of the materials show relatively poor behavior compared to their aged versions, whereas the pristine CF8 material performs noticeably better than its aged versions. It is possible that the thermal

degradation of the other microstructural features in the material is dominating the mechanical properties. Obviously aging does have some effect on this material, but it is unclear that if the ferrite content is high enough to be the driving force or if some other factor is dominant.

Figure 3-6 shows J-R curves for CF8M (~6% δ-ferrite), a high-molybdenum version of CF8. In this plot, the pristine material shows the worst properties while the 400°C material generally shows the best and the other three materials are somewhere in between. This behavior is reflected in the behavior of this material at room temperature, with the material aged at 400°C showing the highest toughness and the pristine material showing only slightly better toughness than the material aged at 360°C. Since the material subjected to the most extreme aging conditions actually shows the best properties at both room temperature and elevated temperature, it can be concluded that at a δ-ferrite content of ~6% the ferrite content is low enough that its spinodal decomposition and embrittlement is not the dominant factor in the effects of aging, at least for this particular material. It would appear that the effects of aging on the other microstructural features are dominant for this material, and those effects provide a toughening rather than embrittling effect.

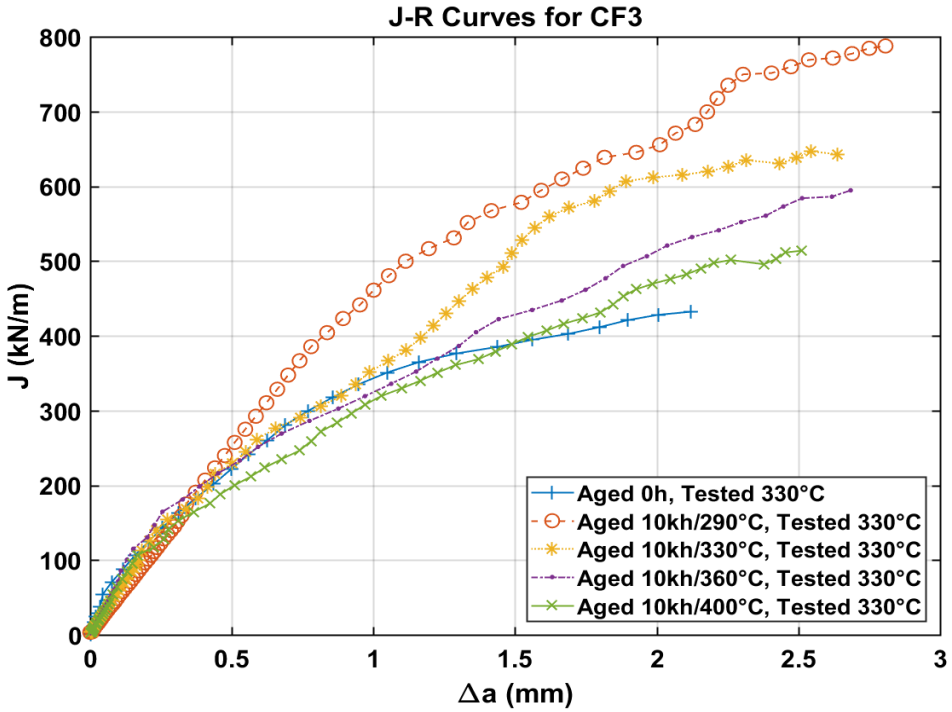

Figure 3-3. Selected J-R curves for the cast alloy CF3, which was aged for 10kh at four different temperatures and tested at 330°C.

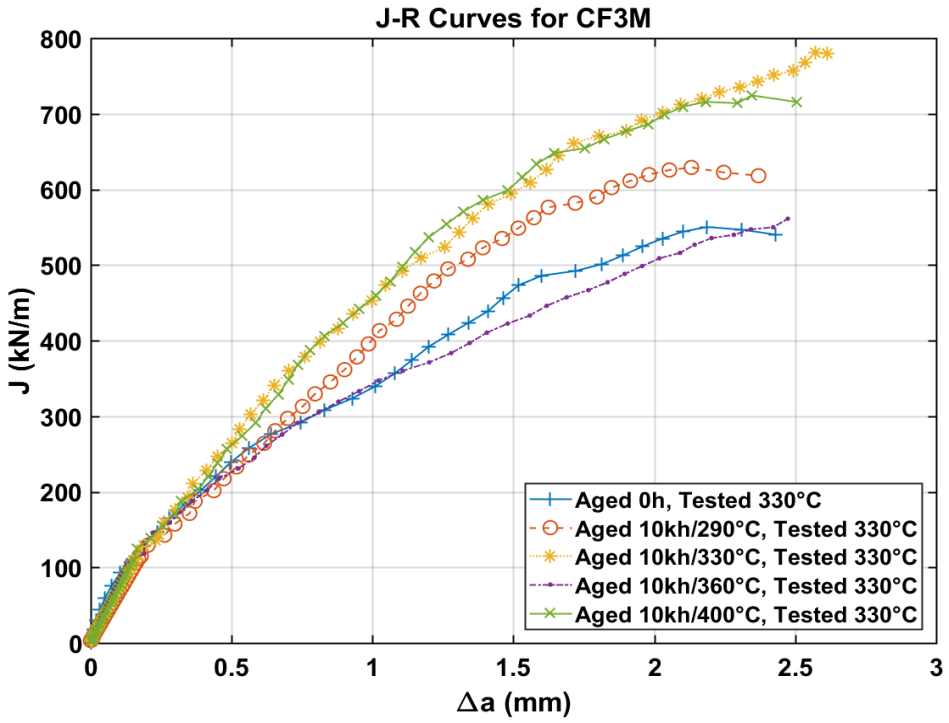

Figure 3-4. Selected J-R curves for the cast alloy CF3M, which was aged for 10kh at four different temperatures and tested at 330°C.

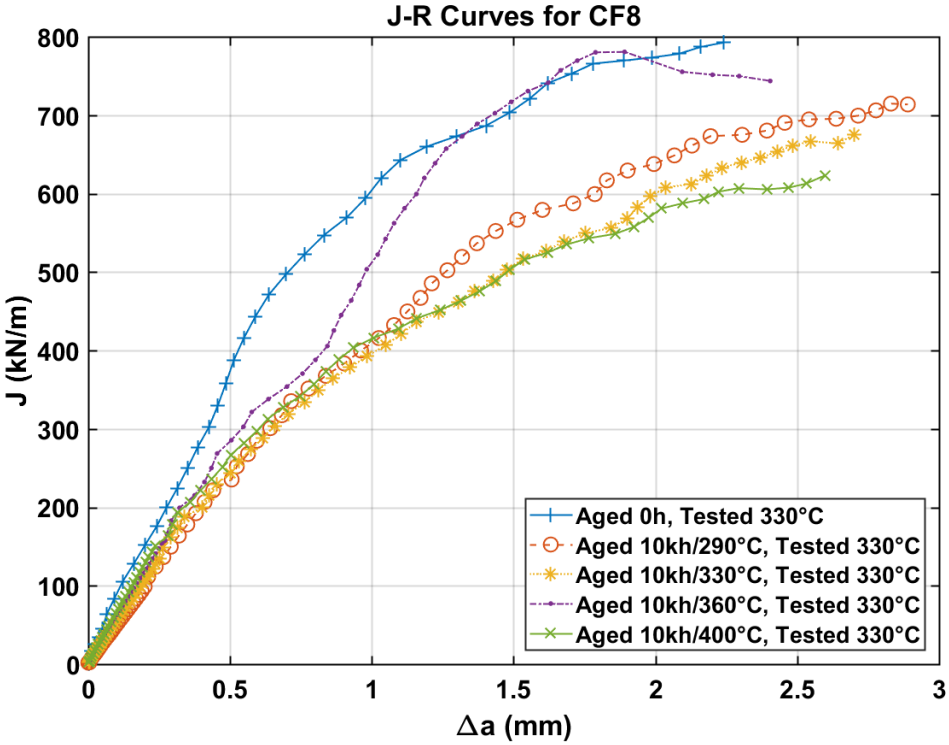

Figure 3-5. Selected J-R curves for the cast alloy CF8, which was aged for 10kh at four different temperatures and tested at 330°C.

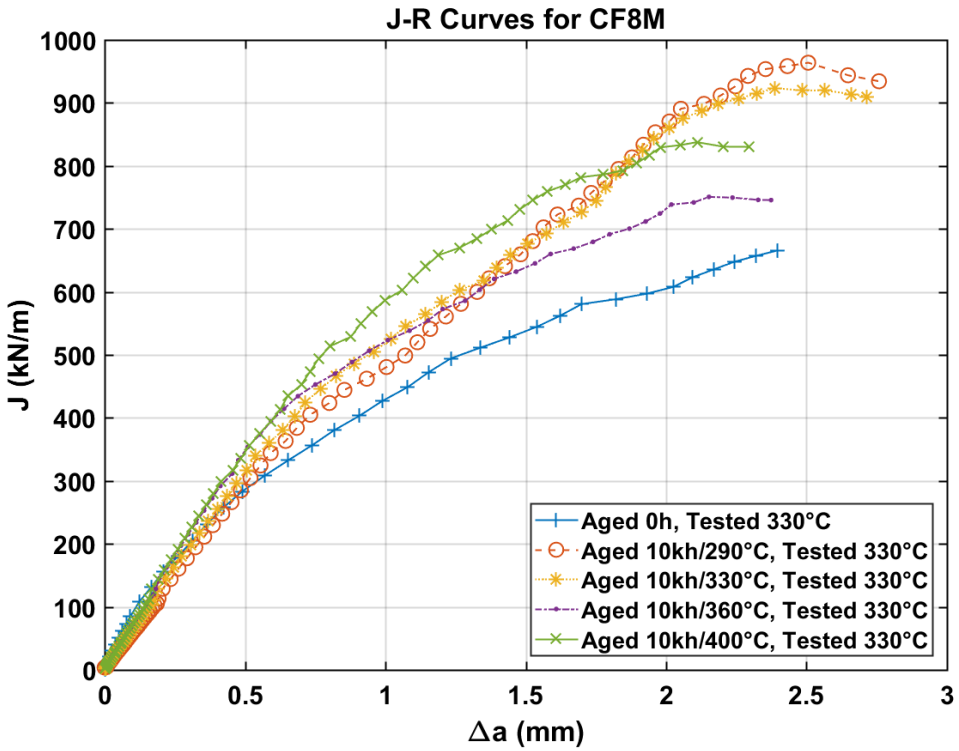

Figure 3-6. Selected J-R curves for the cast alloy CF8M, which was aged for 10kh at four different temperatures and tested at 330°C.

Figures 3-7 through 3-10 display the selected J-R curves of the EPRI-provided CASS materials (CF8 (ELB), CF8M (K23), CF8 (S43), and CF3 (Z21)). These materials contain a wider variety of δ-ferrite content than the model alloys, and therefore the aging effects on fracture resistance are expected to vary more widely. In particular, the static cast alloys with the highest δ-ferrite contents, CF8 (ELB) and CF8 (S43) (~33% and ~25%, respectively), demonstrate more obvious and profound degradation of fracture resistance. The centrifugally cast alloys, CF8M (K23) and CF3 (Z21), show less significant and mixed degradation behavior.

Figure 3-7 compares three J-R curves for the CF8 (ELB) material with ~33% δ-ferrite. All three materials perform better at 330°C than at room temperature, even the pristine material. It seems that the degraded ferrite is still ductile enough at 330°C and hence the 330°C aged material can perform comparably with the pristine material. The 360°C aged material performs significantly more poorly. Although not shown here, the effect of the high ferrite content is highly apparent at room temperature, with the 10kh/360°C material performing very poorly, the pristine material performing reasonably well, and the 10kh/330°C performing somewhere in between. All three materials show a similar temperature dependence on toughness, where the toughness is low at low (RT) and high (400°C) test temperatures, but relatively high at moderate temperatures (290-330°C). However, the more extreme aging a material has undergone, the more noticeably lower its fracture toughness will be relative to the less-aged materials for the same temperature. It appears that with such a high ferrite content the material will become degraded so much that elevating the test temperature cannot improve its fracture toughness.

As can be seen in Figure 3-8, which shows several J-R curves for the alloy CF8M (K23, with

~11% δ-ferrite), the degree of thermal aging in this material is generally indicative of its fracture resistance, with the pristine material performing the best and the more heavily-aged materials performing the worst. It seems obvious that these EPRI-provided materials, which might have enough annealing effects during cooling (i.e., stress relaxation and near-equilibrium phases), demonstrate ageing degradation in a more orderly manner. That is, the property degradation is proportional to the degree of thermal aging. Further, the fine microstructure with a limited amount of ferrite, which resulted from the centrifugal casting, seems to have muted the detrimental effect from high Mo content. With such a non-dramatic degradation in toughness, it is probably better to think of the performance of these materials based on how the curves cluster rather than the individual curves themselves. For example, it can be assumed that a relatively low-aged material will perform comparable to the pristine and 290°C aged materials, whereas a more heavily-aged one will perform similar to the other three; this can be inferred based on the two fairly distinct clusters of the J-R curves for those particular materials. Assuming this, these curves are useful for approximating the performance of a material not explicitly characterized here.

The J-R curves for CF8 (S43, δ-ferrite content ~25%) obtained at 330°Care compared in Figure 3-9. For this static cast material, though its δ-ferrite content is the second highest among the ten alloys, the effects of aging are not particularly noticeable except for the 360°C and 400°C aged materials. It is chemically equivalent to ELB and its performance is remarkably similar—the pristine and 330°C aged material perform roughly the same while the 360°C material does not perform as well, though the difference in performance for this material is less extreme and can probably be attributed to the lower ferrite content relative to ELB. As expected, the 400°C aged material performs the worst. For materials with high ferrite content aged 10kh at 330°C and below, it would seem that at elevated temperatures the performance of the degraded materials is comparable to that of the pristine materials.

Figure 3-10 shows several J-R curves for CF3 (Z21, ~12% δ-ferrite). As with the other low-molybdenum EPRI-provided materials, its performance seems to show that for materials aged at or above 360°C there is a decrease in performance relative to those aged at 330°C, at least for this test temperature (though 10kh/290°C was tested its J-R curve proved difficult to construct, but it showed a very high fracture toughness). An interesting observation for this material is that, although it is chemically and ferrite-content-wise very similar to the model alloy CF3, its fracture toughness for the respective aging conditions is much higher than that of the model alloy version. Indeed, the results in Figures 3-3 and 3-10 contrast the influence of different fabrication routes with very close chemistries: the centrifugal cast Z21 (CF3) demonstrates much better fracture resistance than its static cast counterpart or model alloy CF3. Further, when compared to the 304L alloy with similar chemistry but dissimilar ferrite content, the performance is similar for aging at or below 330°C, but whereas the J-R curves of the 304L cluster closely regardless of aging, there is a noticeable drop in performance for aged 360°C and above. It should be noted that the worst-performing Z21 material shown here performs comparatively to the best-performing model alloy CF3 material shown in Figure 3-3. Despite similar chemistries and ferrite contents these two materials display wildly varying properties—obviously whatever microstructural differences that exist between these two materials, most likely the grain size, are highly influential, and it is likely they have a significant influence on the mechanical properties of the other materials as well.

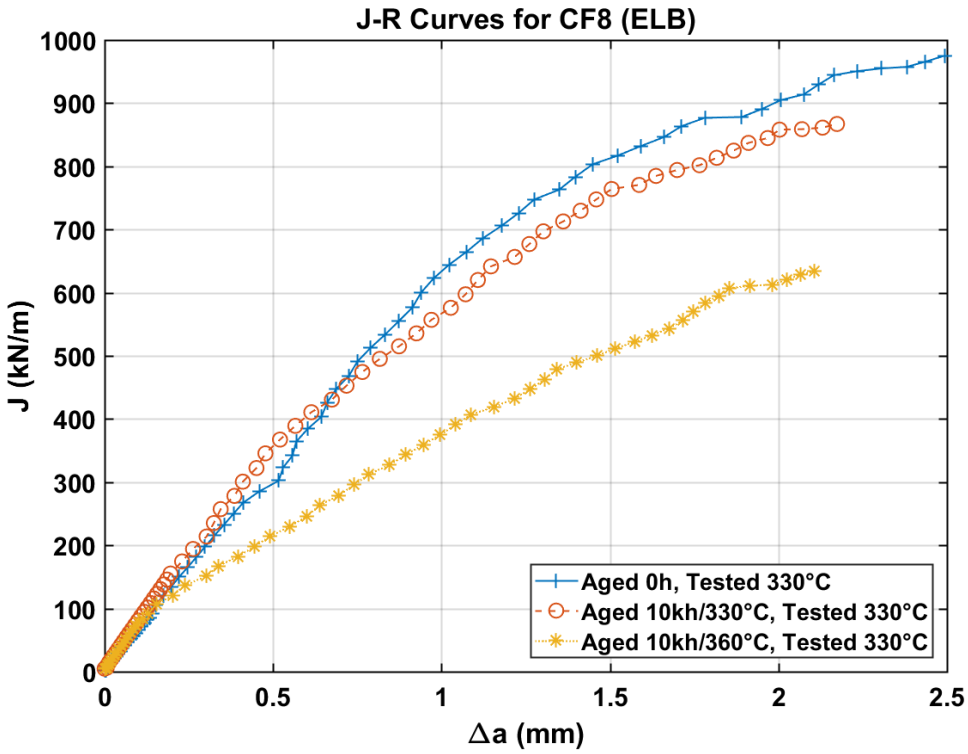

Figure 3-7. Selected J-R curves for the cast alloy CF8 (ELB), which was aged for 10kh at two different temperatures and tested at 330°C.

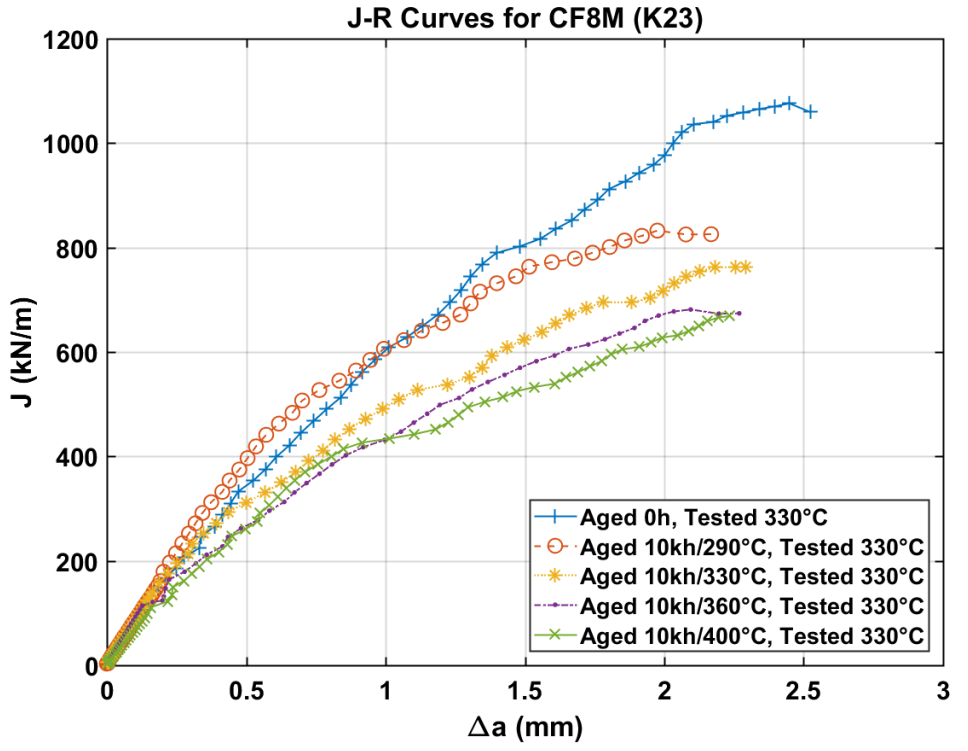

Figure 3-8. Selected J-R curves for the cast alloy CF8M (K23), which was aged for 10kh at four different temperatures and tested at 330°C.

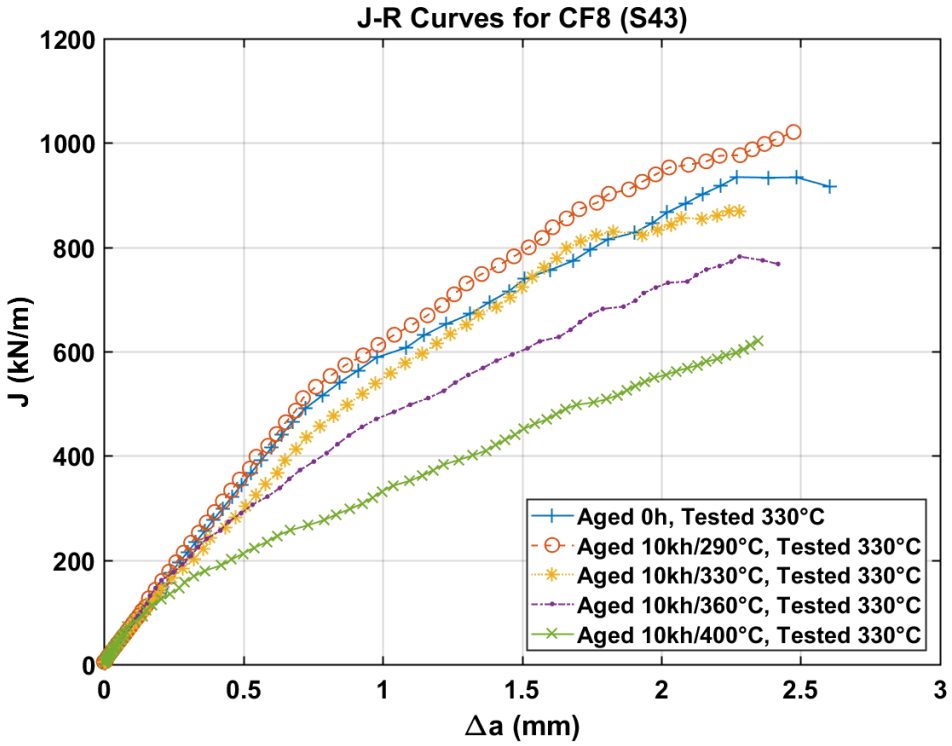

Figure 3-9. Selected J-R curves for the cast alloy CF8 (S43), which was aged for 10kh at four different temperatures and tested at 330°C.

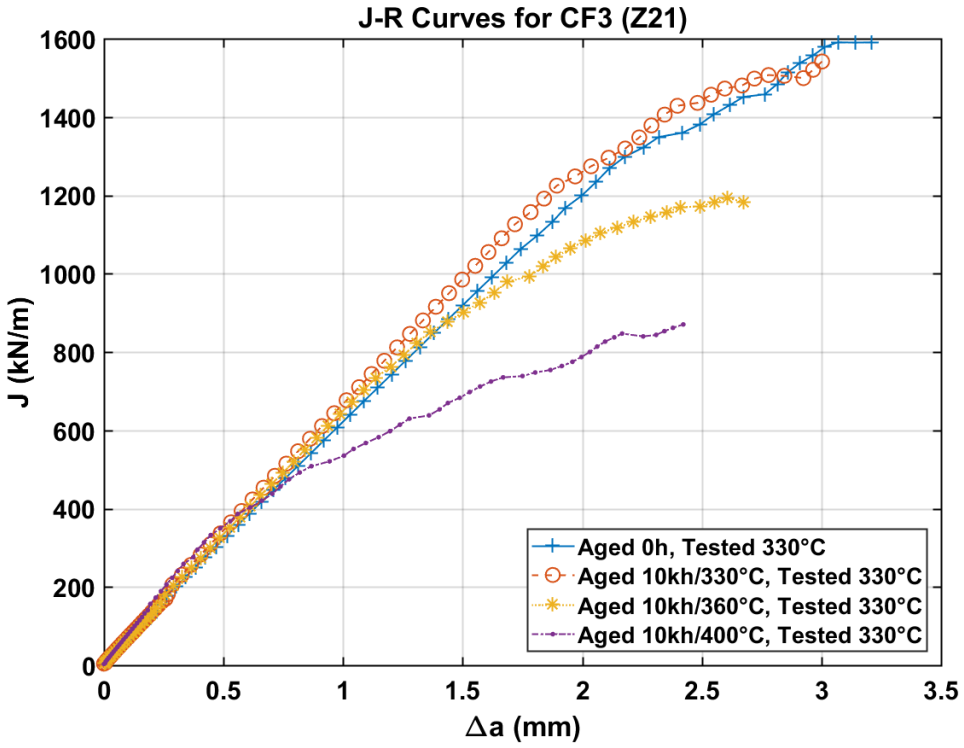

Figure 3-10. Selected J-R curves for the cast alloy CF3 (Z21), which was aged for 10kh at four different temperatures and tested at 330°C.

3.2. Activation energies and a new definition of aging parameter

Thermal aging of cast stainless steels with duplex structures involves multiple major and minor mechanisms in the constituent phases [14-25]. It is known that the spinodal decomposition and G-phase formation in δ-ferrite and segregation and precipitation at interfaces and grain boundaries are the main property degradation mechanisms. Other minor processes such as the stress relaxation in the early aging stage and precipitation of carbide and other phases in austenite and boundaries will also affect the properties. The kinetics of these aging mechanisms will also be vastly different and strongly dependent on aging temperature and alloy composition. Therefore, defining a parameter to measure the degree of thermal aging is not a simple task. Traditionally, the degree of thermal aging has been defined as a measure of aging time at a temperature based on Arrhenius' equation [9]. Arrhenius' equation gives the dependence of the rate constant of a thermally activated reaction on the absolute temperature as well as a pre-exponential factor and other constants of the reaction.

A thermal aging parameter that has been used for the aging of cast stainless steels [9] is defined by

$$P = log_{10} < t \times exp[(-Q/R) * (\frac{1}{T} - \frac{1}{673.15})] >$$

where
t = aging time at temperature T (in K),
Q = activation energy (J/mole),
R = gas constant (8.3145 J/(K·mole)).

This aging parameter P is the logarithm of the aging time at T scaled to the time at 673.15 K (400°C). Since this aging parameter is defined only for aged status, the data of non-aged materials cannot be expressed in the same equation. Also, the aging time scaled to the time of accelerated aging at 400°C is arbitrary and is not related to the reactor operation. In this research, therefore, the aging times are scaled to those at a representative coolant temperature of 325 °C and one (1) is added to the scaled times to avoid having the indefinite value for the non-aged materials. Then, the parameter is defined as

$$A = ln < 1 + t \times exp[(-Q/R) * (\frac{1}{T} - \frac{1}{598.15})] >$$

In this definition of aging parameter, the activation energy (Q) is, again, the most important but highly unknown parameter. The activation energy measured by a specific mechanical property change [26], such as the increase in hardness or decrease in toughness, may not accurately represent the microstructural processes during aging because those macroscopic properties can be influenced both positively and negatively by the effects of the multiple aging processes. Some precipitation mechanisms may soften the phase, which generally helps increase fracture toughness, but may also provide new crack initiation sites, which will lower the toughness value. For instance, some Charpy-impact datasets yielded activation energies in the range of 75–100 kJ/mole, which is well below the average value of ~215 kJ/mole for chromium bulk diffusion, which has been assumed to be rate-controlling in the low-temperature decomposition of the ferritic phase [7,27]. The activation energies for diffusion of metallic elements in the ferrite phase are in the range of 195–250 kJ/mole [27-28]. The activation

energies for Ni and Fe diffusion are known to be, respectively, lower and higher than that of Cr. This Q-range should approximately represent the spinodal decomposition process to form α′ and α phases in various conditions. It was also shown that the activation energies measured for the spinodal decomposition and G-phase precipitation were very similar, and a value of 243±80 kJ/mole was obtained for both mechanisms [26]. Recognizing that these complexities can lead to significant uncertainties when calculating the aging parameter (A), as a gage for the degree of thermal aging, we decided to use the average activation energy measured for chromium bulk diffusion (215 kJ/mole) in the calculation of aging parameter A. Table 3-1 shows the conversion of the aging times at different temperatures to equivalent aging times at 325°C and then to the parameter A.

Table 3-1. Conversion of aging time and temperature to aging parameter A (Q = 215 kJ/mole)

Aging Temp. (°C)	Aging Time (h)	Aging Time at 325°C (h)	Aging Time at 325°C (year)	A
-	0	0	0.00	0.00
290	1500	102	0.01	4.64
330	1500	2147	0.25	7.67
360	1500	16366	1.87	9.70
400	1500	185319	21.16	12.13
290	10000	681	0.08	6.53
330	10000	14310	1.63	9.57
360	10000	109108	12.46	11.60
400	10000	1235458	141.03	14.03

3.3. Fracture toughness versus aging parameter curves

Effects of thermal aging on fracture toughness (K_{JQ}) in two reference wrought alloys are presented in Figures 3-11 and 3-12, in which K_{JQ} is given as a function of A (aging parameter). As listed in Table 3-1, the range of these plots covers practically more than 80 years of reactor operation. Also note that the K_{JQ} data presented in this section, i.e., from the tests at 22°C, 290°C, and 400°C, is less than a half of the total amount of data provided in Appendix-A, the intended purpose here being better clarity in expression and comparison. In these first two plots, all room temperature data seems to fall within the experimental scattering range. Small aging degradations are observed in the data obtained at 290°C and 400°C, but only in the relatively high-A region. For any A, fracture toughness decreases with test temperature. Counting both of these thermally induced decreases, the wrought alloys 304L and 316L retained high fracture toughness well over 400 MPa√m in any tested condition.

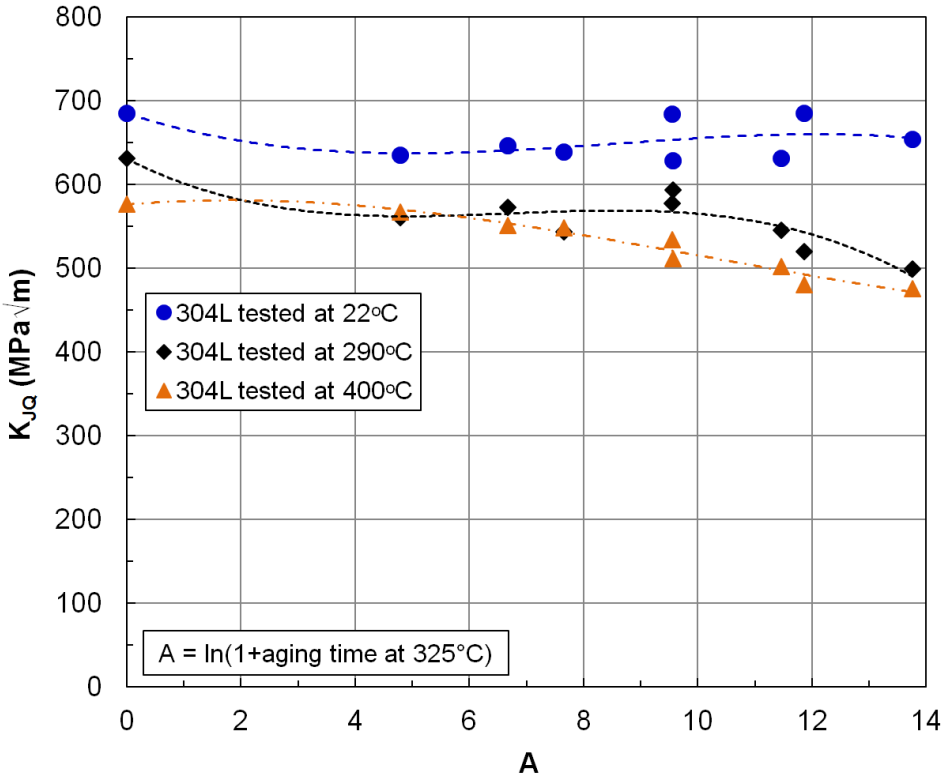

Figure 3-11. Dependence of fracture toughness on the aging parameter for 304L.

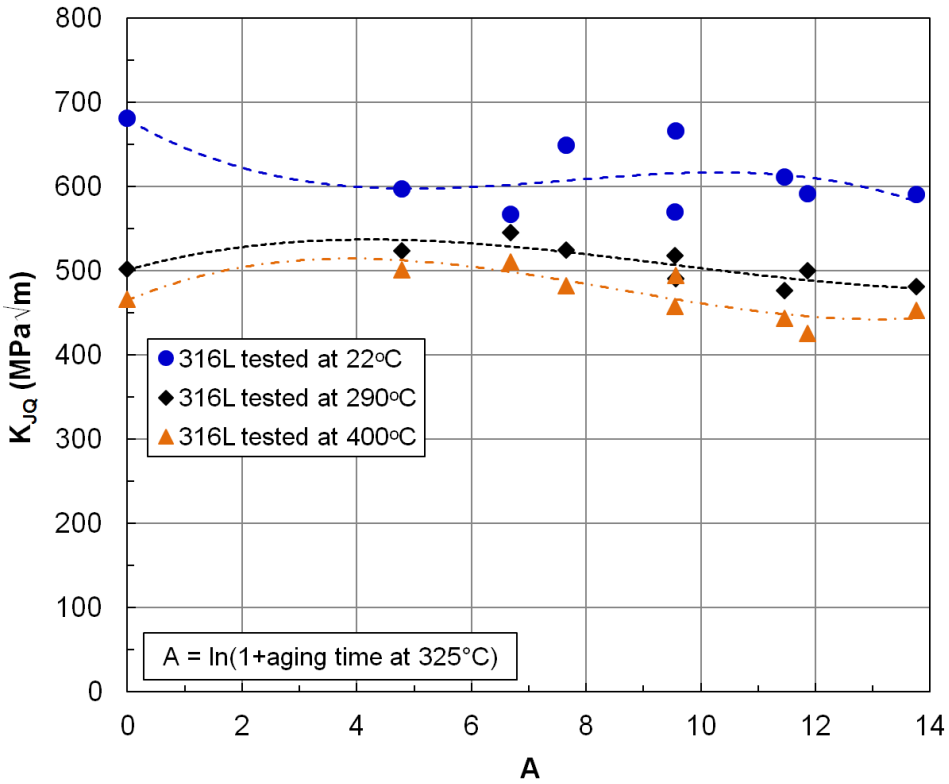

Figure 3-12. Dependence of fracture toughness on the aging parameter for 316L.

Figures 3-13 to 3-16 present the K_{JQ} versus A curves for the four model CASS materials. In Figure 3-13 it is obvious that initial aging ductilizes the cast materials; the non-aged CF3 alloy has a lower fracture toughness than the alloy with the lowest degree of aging (290°C/1.5kh, A = 4.64) at all three test temperatures. The effect of test temperature is more obvious in the lower A region than in the high A region, where no significant test temperature effect is observed. For each test temperature, the initial increase of K_{JQ} is followed by a rapid decrease until A = 11.6, from which K_{JQ} tends to increase. This slight increase of fracture toughness in the highest A region is likely due to over aging or completion of major aging processes. It is notable that, even if the total decrease of K_{JQ} between 4.64 and 11.6 is significant (the room temperature dataset shows a more than 50% reduction), the minimum K_{JQ} values are still respectfully high for such highly aged materials. Over the aging and testing ranges no sign of embrittlement was noticed. Figure 3-14 shows that the dependence of fracture toughness on A for CF3M is similar to that of CF3, except for the highest K_{JQ} at 22°C and A = 0 and the more obvious test temperature dependence in the high A region. As these two static cast materials contain similar amounts of δ-ferrite, ~12% and ~16%, respectively, their overall ranges of K_{JQ} values are also similar.

The model CASS alloys CF8 and CF8M contain small amounts of δ-ferrite, ~5% and ~6% respectively, and accordingly, the dependence of fracture toughness on A appears to be insignificant in these alloys, as seen in Figures 3-15 and 3-16. Further, the dependence of fracture toughness on test temperature depends on the aging parameter region; this dependence is not obvious in these datasets overall. The CF8 alloy, with the lowest ferrite content among the model CASS materials as well as a lower molybdenum content, demonstrates relatively high fracture toughness over the whole A range; it never decreases below ~250 MPa√m. Meanwhile, the fracture toughness data of the CF8M alloy is in similar range, but a few lower values near 200 MPa√m are found at a high A of ~12.

As listed in Table 3-1, the 80 years of CASS component operation at 325°C is within the range of aging parameter A covered in the research. It can be stated, therefore, that the minimum fracture toughness among the data given in these plots, ~200 MPa√m, will be the worst case expected in the extended plant lifetime. In summary, the four model CASS alloys demonstrated high fracture toughness after no or a low degree of thermal aging, and thermal degradation afterwards was not profound. This might be because those alloys contain relatively low δ-ferrite amounts (<16%), and their cooling rates in the casting process were relatively high as their ingot diameters were relatively small (< ~10 cm). This may have led to the formation of fine structures, leading to relatively high fracture toughness and resistance to aging embrittlement.

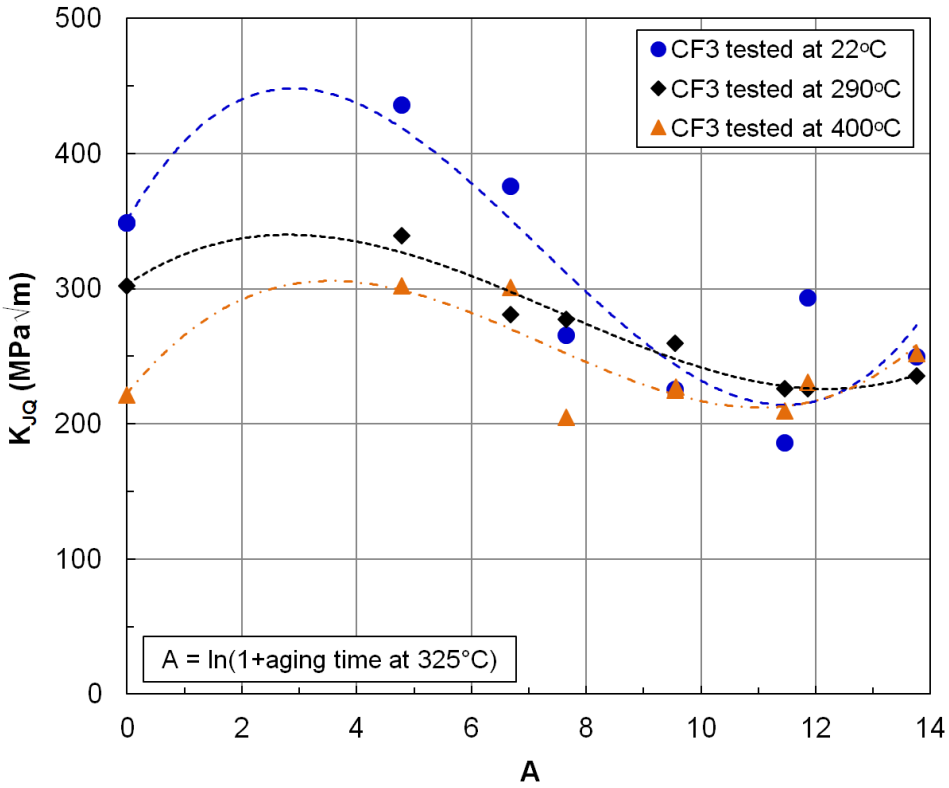

Figure 3-13. Aging parameter dependence of fracture toughness in CF3.

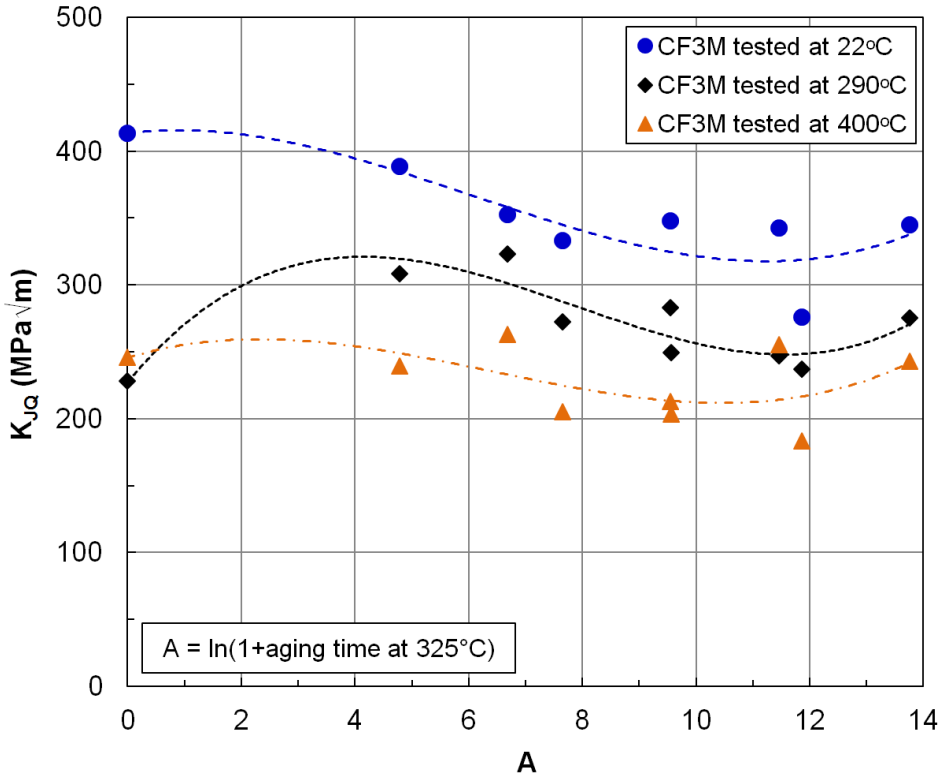

Figure 3-14. Aging parameter dependence of fracture toughness in CF3M.

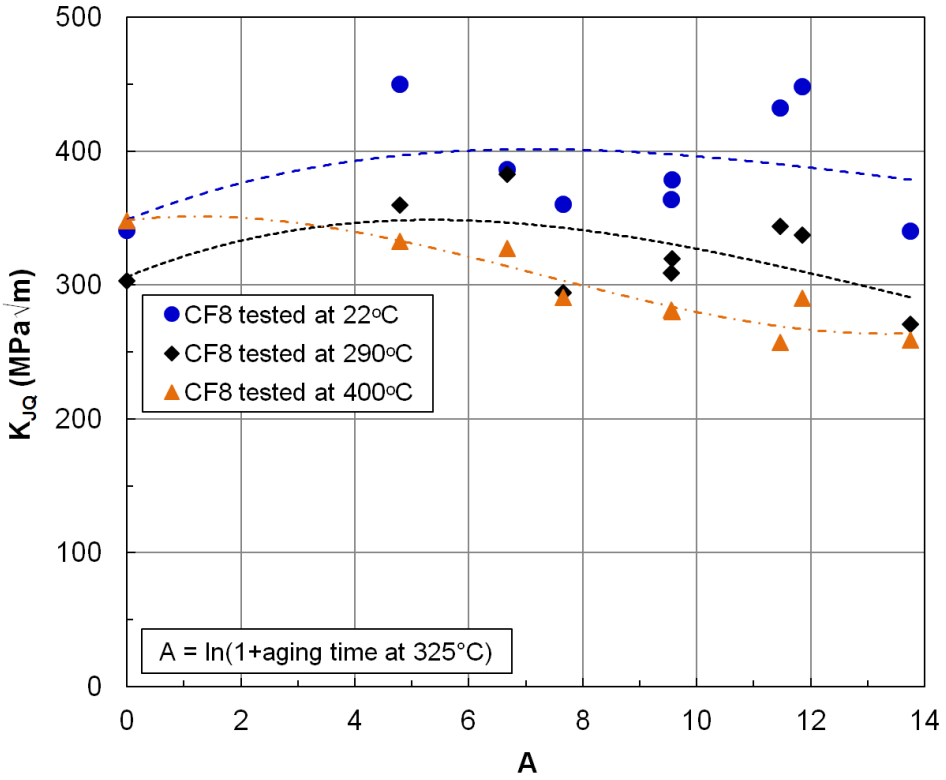

Figure 3-15. Aging parameter dependence of fracture toughness in CF8.

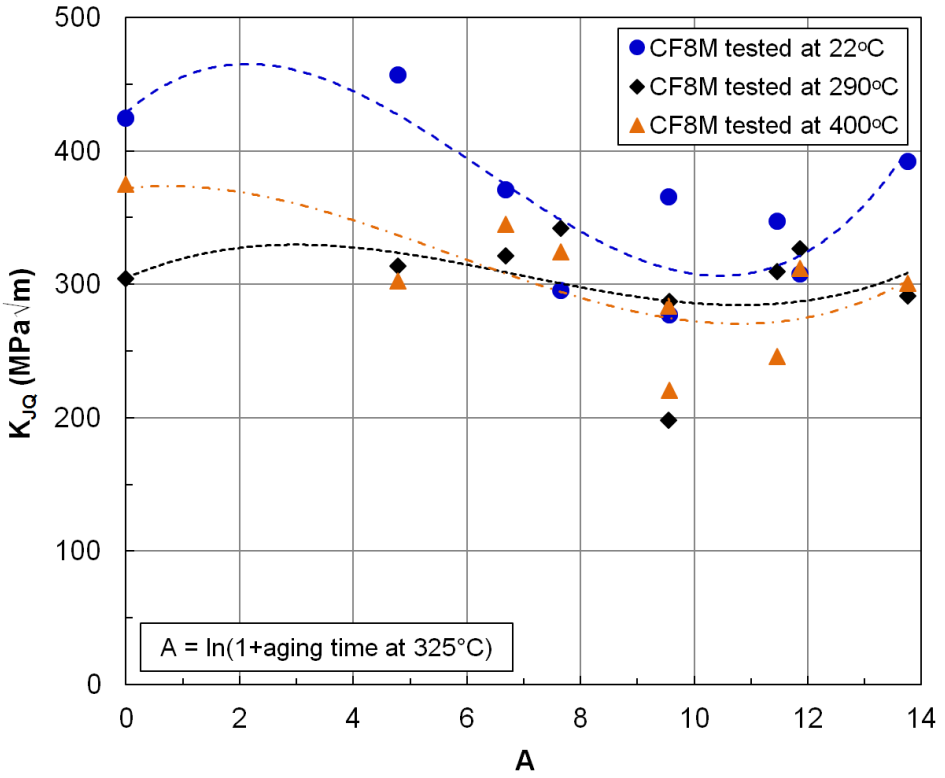

Figure 3-16. Aging parameter dependence of fracture toughness in CF8M.

Figures 3-17 and 3-18 display the K_{JQ} versus A curves for the two static cast materials of the four EPRI-provided materials. Both of these elbow (ELB) and piping (S43) materials have CF8 compositions; their δ-ferrite volume fractions are 33% and 25%, respectively, which were highest among all the materials tested in the research. Because of this, the degradation of fracture resistance and toughness is steepest with these alloys. The CF8 (ELB) alloy shows a steep decrease of K_{JQ} at all test temperatures; in particular, its K_{JQ} at room temperature was mostly lower than at elevated temperatures, and it decreased with A to slightly above 100 MPa√m, below which the alloy would lose capability as a structural material. This poor behavior at room temperature might be because the ELB alloy has relatively low strength due to a coarse microstructure formed during slow cooling in the casting process, and because the unique linear slip, which usually is a preferred deformation mechanism under high stress and can result in high ductility and toughness, was not properly activated in fracture testing. (Note that, because of the limited amount of materilas, the CF8 (ELB) alloy was aged in selected conditions only and therefore the number of K_{JQ} values reported here are also limited. Therefore, the plots in Figure 3-17 might fail to show the possible initial increase of fracture toughness.)

The A-dependence of K_{JQ} for the alloy CF8 (S43) shown in Figure 3-18 resembles that of the model alloys displayed in Figures 3-13, 3-14, and 3-16; there is a clear initial increase of K_{JQ}, followed by a steep decrease, then by a saturation or slight increase at high A values. A few differences are observed as well;the fracture toughness overall is higher in CF8 (S43) than in the model alloys, and the decrease of K_{JQ} is steeper in the A-range of 4–12. Comparing the K_{JQ} versus A plots presented in this report, it is evident that the rate of decrease of fracture toughness in the A-range is dependent on the δ-ferrite content of the alloy.

Figures 3-19 and 3-20 show the effects of aging on the fracture toughness of CF8M (K23) and CF3 (Z21) alloys. Both piping materials were produced through centrifugal casting and have similar amounts of δ-ferrite, 11% and 12% respectively. These δ-ferrite amounts are close to those of static cast model alloys CF3 and CF3M. While the aging effect on K_{JQ} in the CF8M (K23) is close to that of the model alloys, the same effect in CF3 (Z21) seems quite different from that of the static cast model alloys. This might be because the centrifugal cast has produced a finer microstructure in this alloy which can lead to a high fracture toughness. The overall level of K_{JQ} in the Z21 material is highest among the tested cast alloys; the fracture toughness before aging is in the range of 500–800 MPa√m, which is a similar fracture toughness range as that of the wrought alloys, and whilesome steep decreases are found as the aging parameter increases, the K_{JQ} values remained near or above 300 MPa√m at the highest degree of thermal aging.

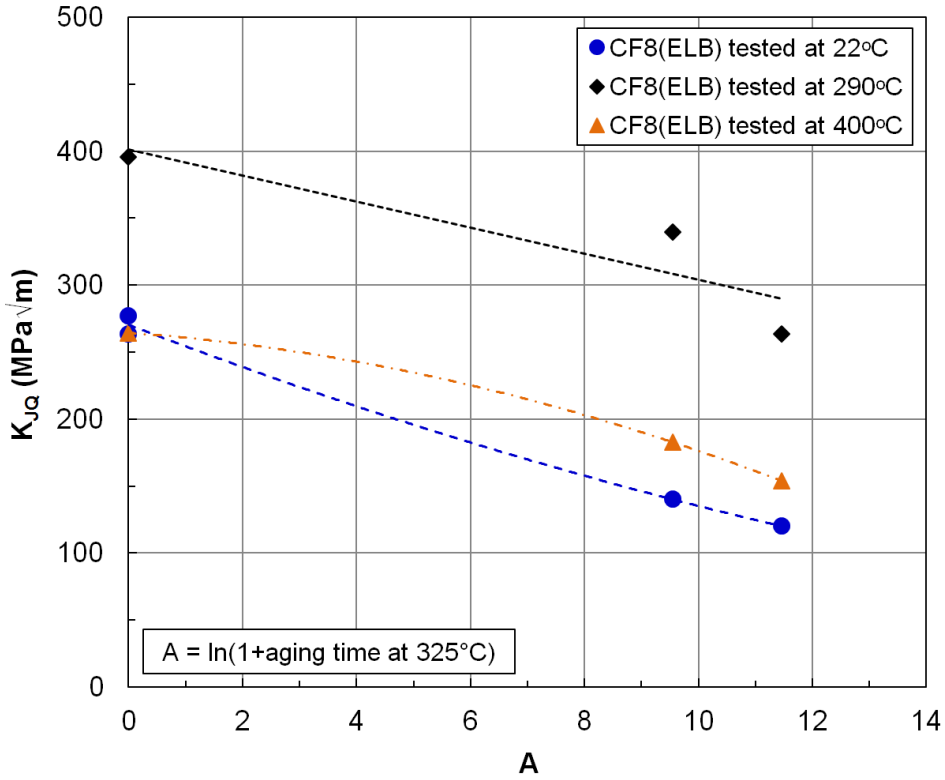

Figure 3-17. Aging parameter dependence of fracture toughness in CF8 (ELB).

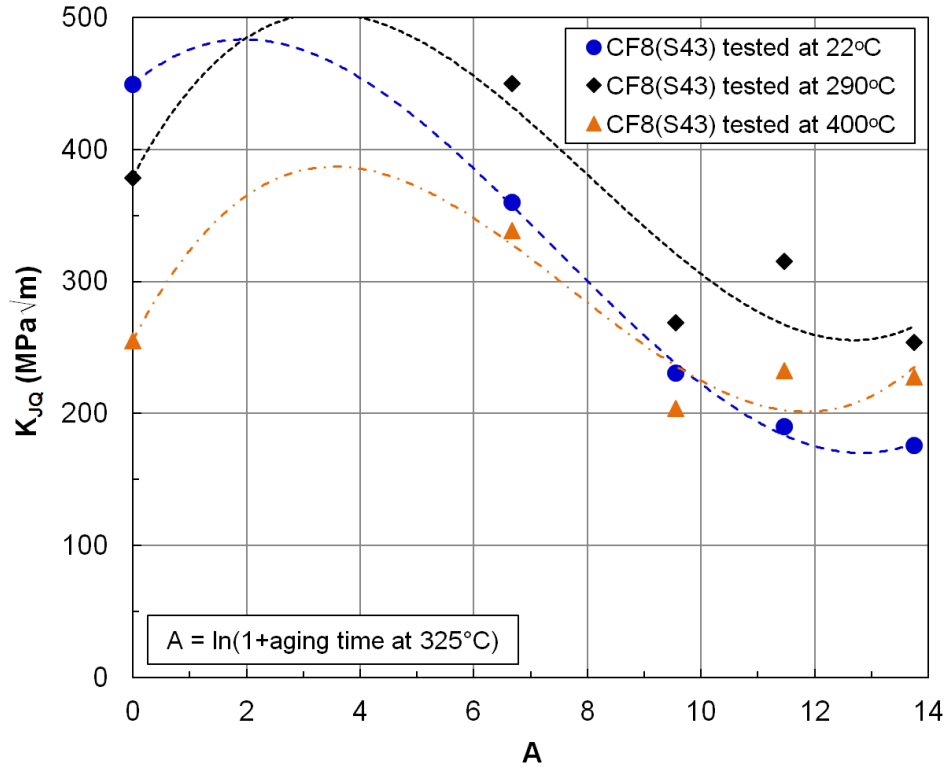

Figure 3-18. Aging parameter dependence of fracture toughness in CF8 (S43).

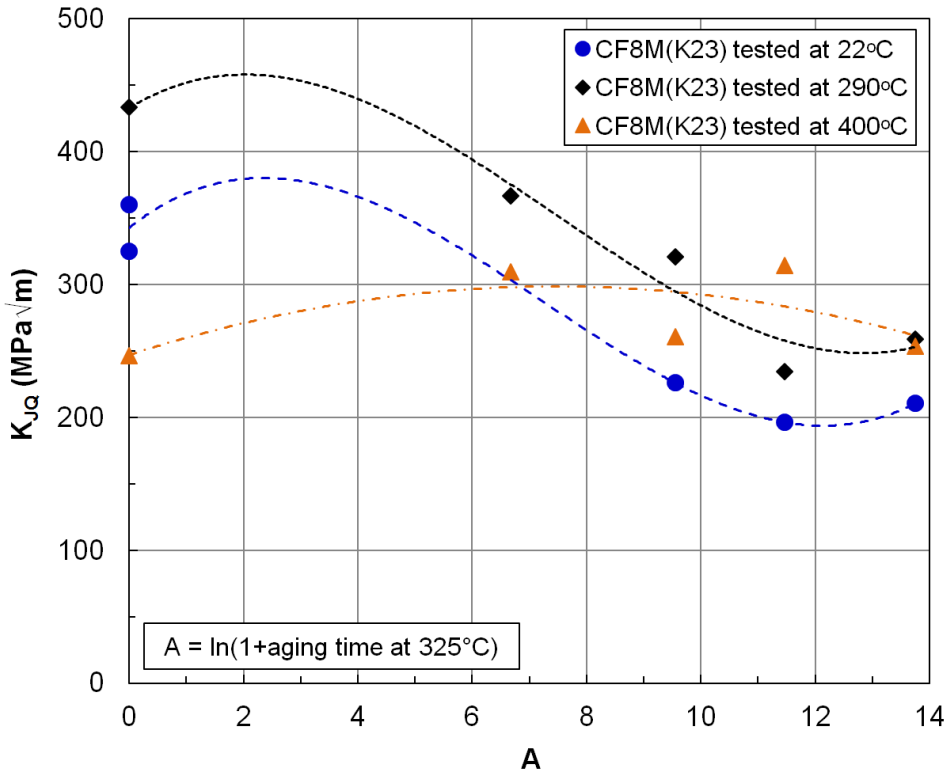

Figure 3-19. Aging parameter dependence of fracture toughness in CF8M (K23).

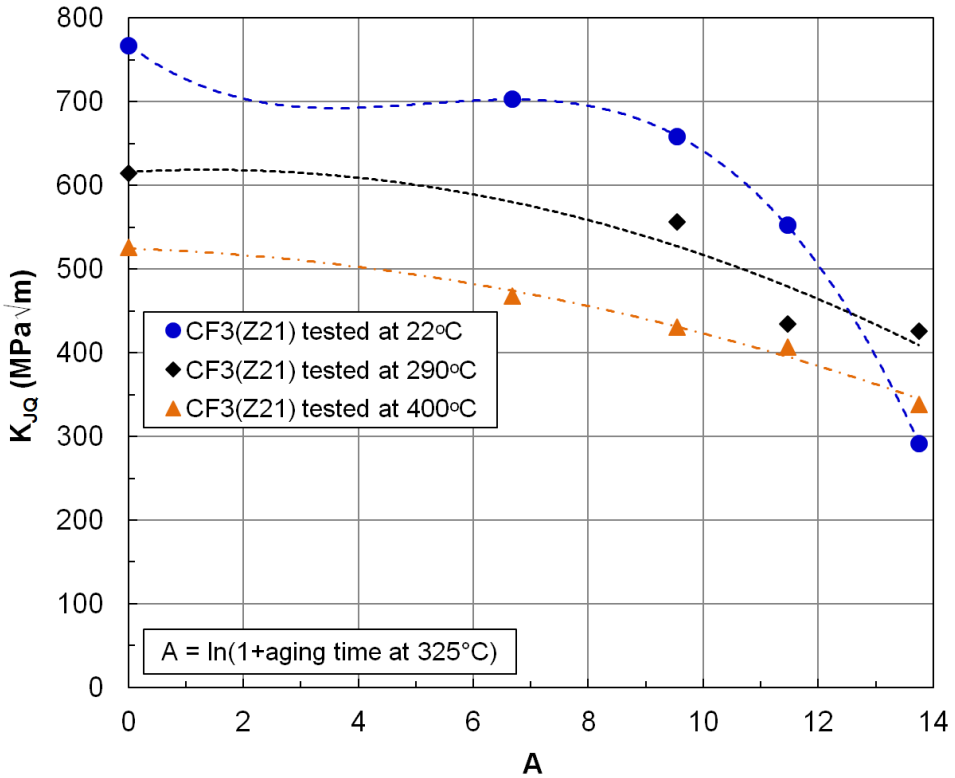

Figure 3-20. Aging parameter dependence of fracture toughness in CF3 (Z21).

4. SUMMARY AND CONCLUSIONS

Fracture toughness has been considered as a key parameter that can directly gage thermal degradation of many large CASS components in nuclear power plants, and retaining high fracture toughness is critical to the structural integrity of the components and entire reactor coolant system. The CASS portfolio in the project includes four model CASSs (CF3, CF3M, CF8, and CF8M) and four EPRI-provided CASSs (CF3, two CF8s, and CF8M). These materials have been thermally aged at 290, 330, 360 and 400°C for more than three years as of today. Two wrought stainless steels, 304L and 316L, have also been aged along with the cast stainless steels to obtain reference degradation data with nearly pure austenitic alloys.

As a main activity of the work scope for the fiscal year, we have carried out testing and evaluation campaign to build a large fracture toughness database for a variety of CASS materials after thermal aging. It was intended that the campaign outcomes would lead to a useful conclusion regarding the possible static fracture of the CASS components in design or extended term operations. Since the start of the project, more than 460 static fracture toughness (J-R) tests have been completed for the eight CASS and two wrought materials aged up to 10 kh and the results are presented in this report. Listed below are the main observations of the campaign:

(1) A new aging parameter (A) was defined to present the aging degradation of mechanical properties against one common variable, which was based on the Arrhenius equation for scaling the aging times between different aging temperatures. For a conversion of aging time (t) and temperature (T) to an aging time at 325 °C, the parameter is given as

$$A = ln < 1 + t \times \exp[(-Q/R) * (\frac{1}{T} - \frac{1}{598.15})] >.$$

(2) Fracture test results indicate that the fracture toughness tends to increase in early aging; after a short time, however, it decreases with aging parameter at a rate depending on the volume fraction of δ-ferrite.

(3) Except for a few cases such as the static cast CF8 (ELB) with the highest δ-ferrite content (33%) and the CF3 (Z21) with extraordinary initial fracture toughness, the decrease of fracture toughness with A appears to stop at a high A of 12 or 14, and in some cases the reincrease of fracture toughness due to overaging induced ductilization is obvious.

(4) The reduction of static fracture toughness due to thermal aging is less significant than that of Charpy impact energy, which usually is measured as the reduction of upper shelf energy and shift of ductile-brittle transition temperature (see M2LW-17OR0402152).

(5) A preliminary conclusion derived for the static fracture behavior of aged CASS materials is that the cast stainless steels with δ-ferrite contents less than ~20% will not be subjected to a significant reduction of static fracture toughness or embrittlement over the extended lifetimes of reactors.

(6) Addition of the data from the 30000 hour aging and further analysis in FY 2019 is expected to help drawing more articulated embrittlement criteria for materials and aging conditions.

REFERENCES

[1] J.T. Busby, P.G. Oberson, C.E. Carpenter, M. Srinivasan, *Expanded Materials Degradation Assessment (EMDA)-Vol. 2: Aging of Core Internals and Piping Systems,* NUREG/CR-7153, Vol. 2, ORNL/TM-2013/532, October 2014.

[2] R. Dyle, *Materials Degradation Matrix and Issue Management Tables Overview-LTO Update* (Presented at the Second Workshop on U.S. Nuclear Power Plant Live Extension, Washington, D.C, 2011).

[3] M. Blair, T.L. Stevens, *Steel Castings Handboo*k, ASM International, 1995.

[4] ASTM A743/A743M-13, *Standard Specification for Castings, Iron-Chromium, Iron-Chromium-Nickel, Corrosion-Resistant, for General Application*.

[5] ASTM A744/A744M-13, *Specification for Castings, Iron-Chromium-Nickel, Corrosion Resistant, for Severe Service*.

[6] ASTM A351/A351M-14, *Standard Specification for Castings, Austenitic, for Pressure-Containing Parts.*

[7] K. Chopra and A. Sather, *Initial Assessment of the Mechanisms and Significance of Low-Temperature Embrittlement of Cast Stainless Steels in LWR Systems (*NUREG/CR–5385, 1990).

[8] K. Chopra, *Effects of Thermal Aging and Neutron Irradiation on Crack Growth Rate and Fracture Toughness of Cast Stainless Steels and Austenitic Stainless Steel Welds* (NUREG/CR-7185, 2014).

[9] K. Chopra, *Estimation of Fracture Toughness of Cast Stainless Steels during Thermal Aging in LWR Systems* (NUREG/CR-4513, 1991).

[10] W.F. Michaud, P.T. Toben, W.K. Soppet, and O.K. Chopra, *Tensile-Property Characterization of Thermally Aged Cast Stainless Steels (*NUREG/CR-6142, 1994).

[11] H.M. Chung and T R. Leax, *Mater. Sci. Technol.* 6, 249–262 (1990).

[12] H.M. Chung, *Evaluation of Aging of Cast Stainless Steel Components* (Presented at ASME Pressure Vessel & Piping Conference, San Diego, CA, 1991).

[13] H.M. Chung, *Presented at the American Society for Mechanical Engineers-Material Properties Council Symposium on Plant Life Extension for Nuclear Components* (Honolulu, Hawaii, 1989).

[14] T.S. Byun, J.T. Busby, *Cast Stainless Steel Aging Research Plan,* ORNL/LTR-2012/440, September 2012.

[15] T.S. Byun, Y. Yang, N.R. Overman, J.T. Busby, *Thermal Aging Phenomena in Cast Duplex Stainless Steels,* JOM, 68(2) (2016) 507-526.

[16] S. Li, Y.L. Wang, H.L. Zhang, S.X. Li, K. Zheng, F. Xue, X.T. Wang, *J Nucl. Mater.* 433, 41 (2013).

[17] M. Murayama, Y. Katayama and K. Hono, *Metall. Mater. Trans. A.* 30A, 345 (1999).

[18] T. Sourmail, *Mater. Sci. Tech.* 17, 1 (2001).

[19] L.P. Stoter, *J. Mater. Sci.* 16, 1039 (1981).

[20] B. Weiss and R. Stickler, *Metal Trans.* 3, 851 (1972).

[21] J.E. Spruiell, J.A. Scott, C.S. Ary, and R.L. Hardin, *Metal Trans.* 4, 1533 (1973).

[22] J. Charles *Proceedings of Duplex Stainless Steel Conference*, Vol 1 (Les Editions de Physique, Les Ulis Cedex, 1991) pp. 3-48.

[23] K.H. Lo, C.H. Shek, J.K.L. Lai, *Mater Sci Eng. R* 65, 39 (2009).

[24] P. Hedström, S. Baghsheikhi, P. Liu, J. Odqvist, *Mater. Sci. Eng. A* 534, 552 (2012).

[25] C. Pareige, S. Novy, S. Saillet, P. Pareige, *J. Nucl. Mater.* 411, 90 (2011).

[26] O.K. Chopra and W. L. Shack, *Degradation of LWR Core Materials due to Neutron Irradiation* (NUREG/CR-7027, 2010).

[27] Z.B. Wang, N.R. Tao, W.P. Tong, J. Lu and K. Lu, *Acta Mater.* 51, 4319 (2003).

[28] Z.B. Wang, N.R. Tao, W.P. Tong, J. Lu and K. Lu, *Defect Diffusion Forum 249, 147 (2006).*

(Additional References)

1. R. Dyle, *Materials Degradation Matrix and Issue Management Tables Overview-LTO Update* (Presented at the Second Workshop on U.S. Nuclear Power Plant Live Extension, Washington, D.C, 2011).
2. Chopra, *Effects of Thermal Aging and Neutron Irradiation on Crack Growth Rate and Fracture Toughness of Cast Stainless Steels and Austenitic Stainless Steel Welds* (NUREG/CR-7185, 2014).
3. K. Chopra and A. Sather, *Initial Assessment of the Mechanisms and Significance of Low-Temperature Embrittlement of Cast Stainless Steels in LWR Systems (*NUREG/CR–5385, 1990).
4. K. Chopra, *Estimation of Fracture Toughness of Cast Stainless Steels during Thermal Aging in LWR Systems* (NUREG/CR-4513, 1991).
5. W.F. Michaud, P.T. Toben, W.K. Soppet, and O.K. Chopra, *Tensile-Property Characterization of Thermally Aged Cast Stainless Steels (*NUREG/CR-6142, 1994).
6. H.M. Chung and T R. Leax, *Mater. Sci. Technol.* 6, 249–262 (1990).
7. H.M. Chung, *Evaluation of Aging of Cast Stainless Steel Components* (Presented at ASME Pressure Vessel & Piping Conference, San Diego, CA, 1991).
8. T.S. Byun and J.T. Busby, *Cast Stainless Steel Aging Research Plan* (ORNL/LTR-2012/440, 2012)
9. H. M. Chung, *Presented at the American Society for Mechanical Engineers-Material Properties Council Symposium on Plant Life Extension for Nuclear Components* (Honolulu, Hawaii, 1989).
10. V. Calonne, A.F. Gourgues, A. Pineau, *Fat. Frac. Eng. Mater. & Stuct.* 27, 31 (2004).
11. K. Chandra, R. Singhal, V. Kain, V.S. Raja, *Mater. Sci. Eng. A 527,* 3904 (2010).
12. J.S. Cheon and I.S. Kim, *J. Nucl. Mater.* 278, 96 (2000).
13. F. Danoix, J.Lacaze, A.Gibert, D.Mangelinck, K.Hoummada, E.Andrieu, *Ultramicroscopy,* 132 193 (2013).
14. J.D. Kwon, S.W. Woo, Y.S. Lee, J.C. Park, Y.W. Park, *Nucl. Eng. Des.* 206, 35 (2001).
15. S. Li, Y. Wang, H. Zhang, S. Li, G. Wang, X. Wang, *J Nucl. Mater.* 441, 337 (2013).
16. S. Li, Y. Wang, X. Wang, Mater. Sci. Eng. A625, 186 (2015).
17. S. Li, Y.L. Wang, H.L. Zhang, S.X. Li, K. Zheng, F. Xue, X.T. Wang, *J Nucl. Mater.* 433, 41 (2013).
18. J.E. May, C.A. Caldas de Souza, P.A. de Paula Nascente, P. Soares, C.M. Lepienski, S.E. Kuri, *Mater. Res.* 13(4), 431 (2010).
19. M. Murayama, Y. Katayama and K. Hono, *Metall. Mater. Trans. A.* 30A, 345 (1999).
20. F. Xuea, Z.X. Wang, G. Shu, W. Yu, H.J. Shi, W. Ti, *Nucl. Eng. Des.* 239, 2217 (2009).
21. T. Yamada, S. Okano, H. Kuwano, *J Nucl. Mater.* 350, 47 (2006).
22. Y.H. Yao, J.F. Wei, Z.P. Wang, *Mater. Sci. Eng.* A 551 (2012) 116– 121
23. X. Lv, S. Li, X. Wang, Y. Wang, Z. Wang, F. Xue, H. Zhang, *Nucl. Eng. Des.* 280, 493 (2014).
24. ASTM A743/A743M-13, *Standard Specification for Castings, Iron-Chromium, Iron-Chromium-Nickel, Corrosion-Resistant, for General Application*.
25. ASTM A744/A744M-13, *Specification for Castings, Iron-Chromium-Nickel, Corrosion Resistant, for Severe Service*.
26. ASTM A351/A351M-14, *Standard Specification for Castings, Austenitic, for Pressure-Containing Parts.*
27. T.S. Byun and I.S. Kim, *J Mater. Sci.* 26, 3917 (1991).
28. T.S. Byun and I.S. Kim, *J Mater. Sci.* 28, 2923 (1993).
29. T. Sourmail, *Mater. Sci. Tech.* 17, 1 (2001).
30. L.P. Stoter, *J. Mater. Sci.* 16, 1039 (1981).
31. B. Weiss and R. Stickler, *Metal Trans.* 3, 851 (1972).
32. J.E. Spruiell, J.A. Scott, C.S. Ary, and R.L. Hardin, *Metal Trans.* 4, 1533 (1973).
33. J. Charles *Proceedings of Duplex Stainless Steel Conference*, Vol 1 (Les Editions de Physique, Les Ulis Cedex, 1991) pp. 3-48.
34. K.H. Lo, C.H. Shek, J.K.L. Lai, *Mater Sci Eng. R* 65, 39 (2009).
35. P. Hedström, S. Baghsheikhi, P. Liu, J. Odqvist, *Mater. Sci. Eng. A* 534, 552 (2012).
36. C. Pareige, S. Novy, S. Saillet, P. Pareige, *J. Nucl. Mater.* 411, 90 (2011).
37. Y. Chen, B. Alexandreanu, and K. Natesan, *Crack Growth Rate and Fracture Toughness Tests on Irradiated Cast Stainless Steels* (ANL-12/56, 2012).
38. O.K. Chopra and W. L. Shack, *Crack Growth Rates and Fracture Toughness of Irradiated Austenitic Stainless Steels in BWR Environment (*NUREG/CR-6960, 2008).
39. O.K. Chopra and W. L. Shack, *Degradation of LWR Core Materials due to Neutron Irradiation* (NUREG/CR-7027, 2010).
40. O.K. Chopra and A. S. Rao, *J. Nucl. Mater.* 412 ,195 (2011).
41. Z.B. Wang, N.R. Tao, W.P. Tong, J. Lu and K. Lu, *Acta Mater.* 51, 4319 (2003).

42. Z.B. Wang, N.R. Tao, W.P. Tong, J. Lu and K. Lu, *Defect Diffusion Forum 249, 147 (2006).*
43. L. Kaufman, B. Uhrenius, D. Birnie, K. Taylor, *CALPHAD*, 8, 25 (1984).
44. Y. Yang and J.T. Busby, J Nucl. Mater. 448, 282 (2014).
45. W. Cao, S.-L. Chen, F. Zhang, K. Wu, Y. Yang, Y. A. Chang, R. Schmid-Fetzer, W. A. Oates, *CALPHAD*, 33, 328 (2009).
46. T. S. Byun and Y. Yang, *Baseline Characterization of Cast Stainless Steels* (ORNL/TM-2014/446, 2014)
47. J. Barcik, *Mater. Sci. Tech.* 4, 5 (1988).
48. I. Shuro, H.H. Kuo, T. Sasaki, K. Hono, Y. Todaka, M. Umemoto, Mater. Sci. Eng. A 552, 194 (2012).